Article

# Engineering of ATP synthase for enhancement of proton-to-ATP ratio

Hiroshi Ueno [1] ✉, Kiyoto Yasuda[1], Norie Hamaguchi-Suzuki[2,3], Riku Marui[1], Naruhiko Adachi [4,5], Toshiya Senda [4], Takeshi Murata [2] & Hiroyuki Noji [1] ✉

F_oF_1-ATP synthase (F_oF_1) interconverts the energy of the proton motive force (*pmf*) and that of ATP through the mechanical rotation. The H^+/ATP ratio, one of the most crucial parameters in bioenergetics, varies among species due to differences in the number of H^+-binding c-subunits, resulting in H^+/ATP ratios ranging from 2.7 to 5. In this study, we seek to significantly enhance the H^+/ATP ratio by employing an alternative approach that differs from that of nature. We engineer F_oF_1 to form multiple peripheral stalks, each bound to a proton-conducting a-subunit. The engineered F_oF_1 exhibits an H^+/ATP ratio of 5.8, surpassing the highest ratios found in naturally occurring F_oF_1s, enabling ATP synthesis under low *pmf* conditions where wild-type enzymes cannot synthesize ATP. Structural analysis reveals that the engineered F_oF_1 forms up to three peripheral stalks and a-subunits. This study not only provides valuable insights into the H^+-transport mechanism of F_oF_1 but also opens up possibilities for engineering the foundation of cellular bioenergetics.

F_oF_1-ATP synthase (F_oF_1) is a ubiquitous enzyme found in the membranes of mitochondria, chloroplasts and bacteria. It synthesizes ATP from ADP and inorganic phosphate (Pi) coupled with proton translocation across membranes along the proton motive force (*pmf*)[1–3]. F_oF_1 is a unique molecular motor complex composed of two rotary molecular motors: F_1 and F_o[1,2]. Bacterial F_oF_1 exhibits the simplest subunit composition of $a_1b_2c_x$ (*x* varies among species) for F_o and $\alpha_3\beta_3\gamma_1\delta_1\epsilon_1$ for F_1[4–6] (Fig. 1a). F_o is a membrane-embedded molecular motor driven by *pmf*. When protons are translocated through the proton pathway in F_o along *pmf*, the multimeric rotor ring composed of c-subunits (termed c-ring) rotates against stator ab_2 (Fig. 1a, b). F_1 is the catalytic core domain of F_oF_1 for ATP synthesis and hydrolysis[7]. When isolated from F_o, F_1 acts as an ATP-driven molecular motor that rotates the γε rotor complex against the catalytic $\alpha_3\beta_3$ stator ring coupled with ATP hydrolysis[8]. These two motors are coupled via two stalks: the peripheral stalk, composed of the b_2 dimer stalk and the δ subunit. The central rotor stalk is composed of a γε complex and a c-ring. Under ATP synthesis conditions where *pmf* is sufficient and the rotational torque

of F_o exceeds that of F_1, F_o rotates the γε complex in F_1 in the reverse direction of ATP hydrolysis, driving the ATP synthesis reaction on the $\alpha_3\beta_3$ ring[9,10]. Conversely, when the torque of F_1 exceeds that of F_o, F_1 rotates the c-ring in F_o, forcing F_o to pump protons in the reverse direction, thereby generating *pmf*. Thus, F_oF_1 interconverts the *pmf* and chemical potential of ATP hydrolysis through mechanical rotation.

Considering the Gibbs free energy of this coupling reaction ($\Delta G'$),

$$ADP + Pi + nH_{in}^+ \rightleftharpoons ATP + H_2O + nH_{out}^+ \tag{1}$$
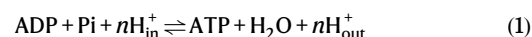
$\Delta G'$ is givens:

$$\Delta G' = \Delta G'_{ATP} - nF \cdot pmf \tag{2}$$

where $\Delta G'_{ATP}$ is the Gibbs free energy of ATP synthesis, F is Faraday's constant, n is the H^+/ATP ratio, which is defined as the number of protons translocated through F_o coupled with a single turnover of ATP synthesis on F_1. Hence, the following conditions must be satisfied to

[1]Department of Applied Chemistry, Graduate School of Engineering, The University of Tokyo, Tokyo, Japan. [2]Department of Chemistry, Graduate School of Science, Chiba University, Chiba, Japan. [3]Department of Pharmacology, Graduate School of Medicine, Chiba University, Chiba, Japan. [4]Structural Biology Research Center, Institute of Materials Structure Science, High Energy Accelerator Research Organization (KEK), Ibaraki, Japan. [5]Life Science Center for Survival Dynamics, Tsukuba Advanced Research Alliance (TARA), University of Tsukuba, Ibaraki, Japan. ✉e-mail: hueno@g.ecc.u-tokyo.ac.jp; hnoji@g.ecc.u-tokyo.ac.jp
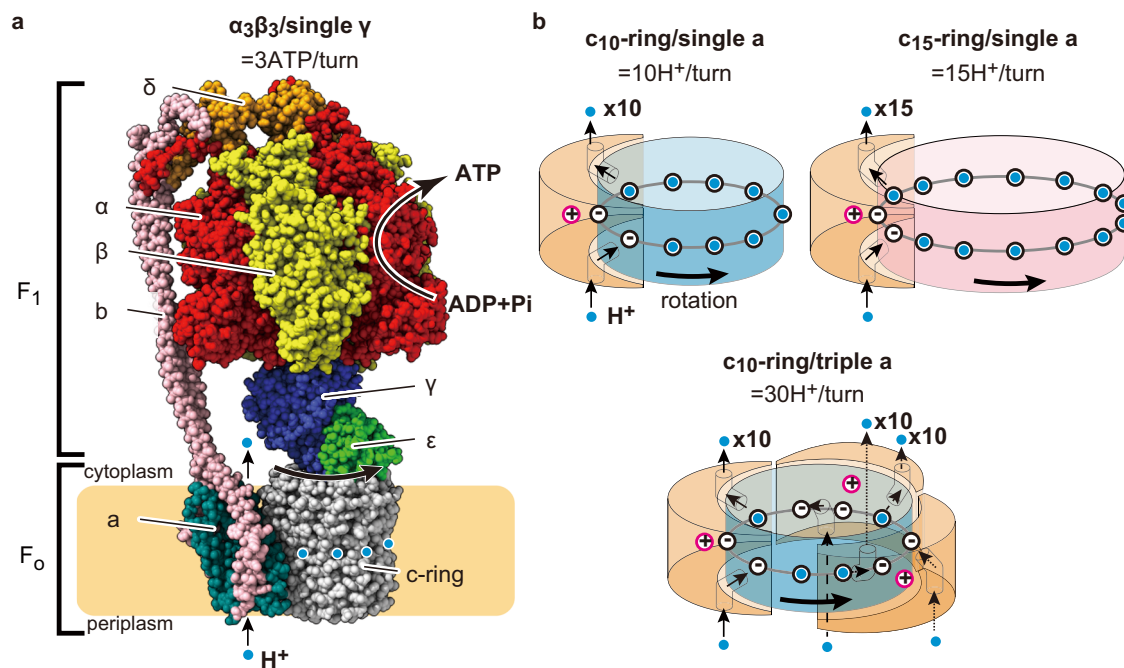
Fig. 1 | Structure of F_oF_1-ATP synthase and rotation mechanism of F_o with a different number of the c-/a-subunits. a Bacterial ATP synthase (from thermophilic *Bacillus* PS3) consists of F_1 ($\alpha_3\beta_3\gamma\delta\varepsilon$) and F_o (ab_2c_{10}) motors. As F_1 has three catalytic sites, three ATP molecules are synthesized per turn of the rotor subunits ($\gamma\varepsilon c_{10}$) against the stator subunits ($\alpha_3\beta_3\delta ab_2$) during ATP synthesis. **b** Models of proton translocation through F_o coupled with the rotation of the c-ring. The highly conserved arginine residues of the a-subunit and glutamate (or aspartate) residues of c-subunits are depicted with pink and black open circles, respectively. Protons are depicted as light blue circles. In the models of c_{10}-ring/single a-subunit and c_{15}-ring/single a-subunit, 10 and 15 protons, equal to the number of the c-subunits, are transferred in one turn, respectively. Conversely, in the c_{10}-ring and triple a-subunits model, a total of 30 protons, equal to the number of the c-subunits multiplied by the number of the a-subunits, are transferred in one turn.

drive ATP synthesis:

$$\Delta G'_{ATP} < nF \cdot pmf \qquad (3)$$

Thus, the H$^+$/ATP ratio is the critical factor in determining the lower limit of *pmf* required for ATP synthesis, given that $\Delta G'_{ATP}$ does not largely vary among species. The H$^+$/ATP ratio is principally defined by the ratio of the reaction stoichiometry of F_o per turn of the rotor complex to that of F_1, and the ratio of H$^+$/turn of F_o to ATP/turn of F_1. All the F_1s studied so far, without exception, have three catalytic β subunits and couple three reactions of ATP hydrolysis/synthesis per turn, defining the ATP/turn ratio as 3[10]. The reaction stoichiometry of F_o, H$^+$/turn varies among species due to differences in the number of c-subunits in the c-ring. According to the half-channel model, supported by recent structural studies, the H$^+$ pathway in F_o is formed by the c-ring and the a-subunit, which has two half-channels exposed to the periplasmic or cytoplasmic side of the membrane[11–13]. During ATP synthesis, H$^+$ from the periplasmic solution enters the half-channel exposed to the periplasmic space and is transferred to one of the c-subunits in the c-ring. Following one revolution of the c-ring, H$^+$ is released into the cytoplasmic solution through the opposite half-channel (Fig. 1b, Supplementary Fig. 1). Thus, the half-channel model assumes that the stoichiometry of H$^+$/turn is determined by the number of c-subunits.

The number of c-subunits in the c-ring in F-type ATP synthases ranges from 8 to 15, depending on the species[14–16]. When assuming perfect energy coupling between F_1 and F_o, the H$^+$/ATP ratio should vary between 2.7 and 5.0 among the species. Various groups have attempted to experimentally determine the H$^+$/ATP ratio from the biochemical measurements of the thermodynamic equilibrium point where the *pmf* and $\Delta G'_{ATP}$ are balanced. The *Bacillus* PS3 F_oF_1, with a c_{10}-ring, has been reported to show good agreement with the structurally expected H$^+$/ATP ratio of 3.3[17]. F_oF_1s from *E. coli* and yeast mitochondria, both of which also have the c_{10}-ring, exhibit slightly different H$^+$/ATP ratios: 4.0 ± 0.3[18] and 2.9 ± 0.2[19], respectively. For spinach chloroplast F_oF_1 with the c_{14}-ring, two independent studies reported smaller values for the H$^+$/ATP ratio: 4.0 ± 0.2[18] and 3.9 ± 0.3[19], which are lower than the expected value of 4.7. Thus, the experimentally determined H$^+$/ATP ratios are close to, but not always identical to, the structurally expected values, varying within a narrow range of 3 to 4.

The H$^+$/ATP ratio of F_oF_1 is one of the most critical parameters in the bioenergetic system of cells, which defines the energy cost of ATP synthesis and the threshold *pmf* required for ATP synthesis (see Eq. 3)[14,17]. Since $\Delta G'_{ATP}$ does not largely differ across organisms, F_oF_1 with a higher H$^+$/ATP ratio can synthesize ATP even at a lower *pmf*. In fact, alkaliphilic bacteria living in highly alkaline environments and photosynthetic organisms that grow under light-limiting conditions have a c-ring with a large number of c-subunits[20–22]. This is thought to be an evolutionary adaptation that allows stable ATP synthesis under low and/or unstable *pmf* conditions[22,23]. Thus, organisms may have optimized the H$^+$/ATP ratio through evolution by tuning the stoichiometry of the c-ring to meet their energetic requirements.

Conversely, when reconsidering the half-channel mechanism, we can assume that the stoichiometry of H$^+$/turn in F_o is determined not only by the number of c-subunits but also by the number of a-subunits (Fig. 1b, bottom). In particular, the F_o structures solved so far show that a large portion of the c-ring is exposed to the lipid bilayer, suggesting the possibility of accommodating one or two additional a-subunits, although F_oF_1 with multiple a-subunits has not yet been identified.

Here, we explore the possibility of doubling or tripling the H$^+$/ATP ratio of F_oF_1 by increasing the number of a-subunits in F_o, rather than increasing the stoichiometry of the c-ring as observed in nature.
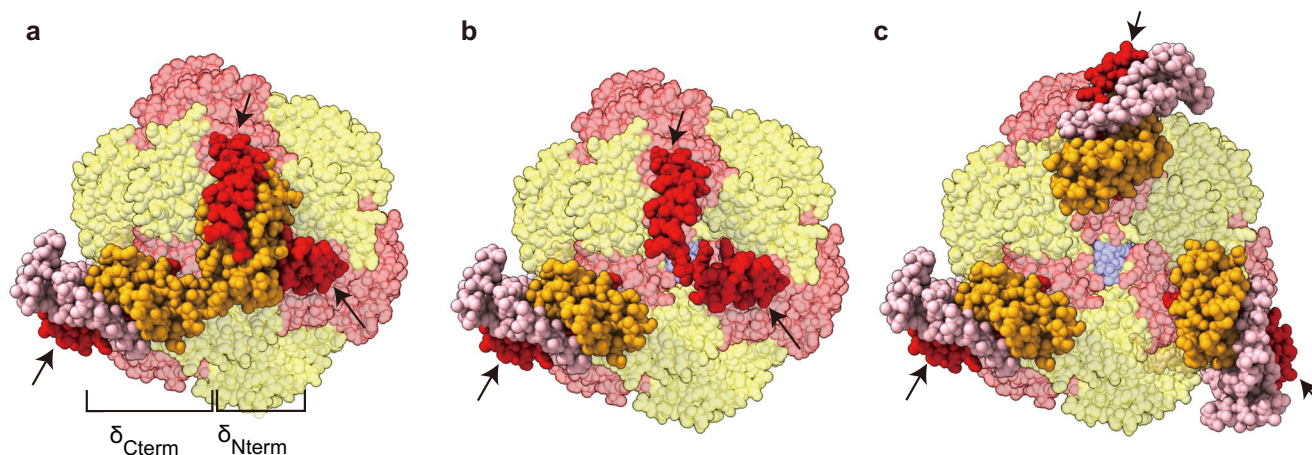
Fig. 2 | Design strategy to multiply peripheral stalks. Top views of *Bacillus* PS3 F_oF_1 from the cytoplasm (PDB ID: 6N2Y). The α (red), β (yellow), γ (blue), δ subunits (orange), and the b_2 stalk (pink) are shown. The non-transparent red parts indicated by the arrows represent the N-terminal region (residues 2–30) of the α subunit. **a** Asymmetric interactions between the δ and α subunits. The single δ subunit interacts with the three α subunits, occupying the central concavity of the $α_3β_3$ subcomplex. **b** Model structure after deletion of the N-terminal domain (residues 2–104) of the δ subunit. The central concavity is exposed, and two of three α subunits are unoccupied. **c** Model structure after each of the N-terminus of the three α subunits is fused to the C-terminal domain (residues 105–178) of the δ subunit.

Results

Design for multiple peripheral stalks

So far, all ATP synthases have a single copy of the a-subunit per F_oF_1 complex. Considering that the a-subunit is tightly bound to the membrane portion of the peripheral stalk, the key factor for multiplying the a-subunits should be the structural mechanism that limits the number of peripheral stalks. The peripheral stalk of the b_2 dimer extends from the membrane to the upper surface of the $α_3β_3$ subcomplex of F_1, binding to the δ subunit. The δ subunit binds to the top of the $α_3β_3$ subcomplex, associating with the N-terminal regions of the three α subunits. One α subunit interacts with the C-terminal region of the δ subunit, while the other two interact with the N-terminal region of the δ subunit, as indicated by the arrows in Fig. 2a. Since the N-terminal domain of the δ subunit is located in the central concavity of the $α_3β_3$ ring, occupying the pseudo-threefold symmetry axis of the $α_3β_3$ ring, it is reasonable to assume that the N-terminal domain of the δ subunit disrupts the pseudo-threefold symmetry, limiting the stoichiometry of the peripheral stalk to one (Fig. 2a). We hypothesized that by removing the N-terminal domain of the δ subunit (Fig. 2b), it becomes possible to accommodate a truncated δ subunit on each α subunit (Fig. 2c). A possible concern regarding the truncation is that the truncated δ subunit ($δ_{ΔN}$) does not form a stable complex with the $α_3β_3$ ring. Therefore, we designed the $δ_{ΔN}$-α fusion construct of *Bacillus* PS3 F_oF_1, where the C-terminus of the δ subunit was genetically fused to the N-terminus of the α subunit. In addition, the inhibitory C-terminal domain of the ε subunit was removed to enhance enzymatic activity[17,24]. In this study, *Bacillus* PS3 F_oF_1-$ε_{ΔC}$ was used as a wild-type F_oF_1 for comparison.
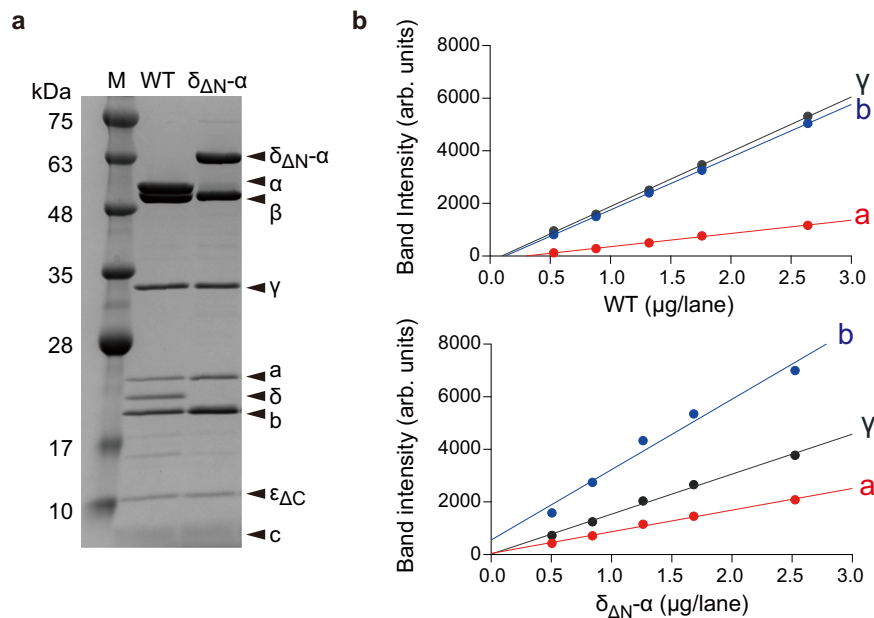
SDS-PAGE analysis of subunit stoichiometry

The $δ_{ΔN}$-α fused F_oF_1 was purified following a previously reported procedure for the wild-type *Bacillus* PS3 F_oF_1[17]. To estimate the subunit stoichiometry, the $δ_{ΔN}$-α fused F_oF_1 was analyzed by SDS-PAGE with the wild-type F_oF_1 for comparison (Fig. 3a, b). The $δ_{ΔN}$-α fused F_oF_1 lacked δ and α, and the $δ_{ΔN}$-α fusion appeared above the band position for the α subunit (Fig. 3a). The $δ_{ΔN}$-α fused F_oF_1 retained the complete set of subunits. Then, we estimated the subunit stoichiometry of the a- and b-subunits in the $δ_{ΔN}$-α fused F_oF_1 by using the γ subunit as the internal reference in comparison with the wild-type (Fig. 3b, Supplementary Fig. 2). In the wild-type, the b-subunit exhibited a band intensity

comparable to that of the γ subunit, whereas in the $δ_{ΔN}$-α fused F_oF_1, the b-subunit showed higher signals relative to the γ subunit. Similarly, the $δ_{ΔN}$-α fused F_oF_1 exhibited a higher band intensity for the a-subunit compared to the wild type, indicating that the $δ_{ΔN}$-α fused F_oF_1 increases the stoichiometry of the a- and b-subunits. For a more quantitative estimation, we plotted calibration lines for the wild-type and mutant subunits and standardized the lines using the γ subunit calibration lines as the internal control (Fig. 3b). We then determined the stoichiometries of the a- and b-subunits in the $δ_{ΔN}$-α fused F_oF_1 by comparing them to the wild-type. The estimated stoichiometries of the a- and b-subunits were 2.2 and 1.8 times higher than those of the wild-type F_oF_1, respectively (see Fig. 3b legend). Thus, it was confirmed that the $δ_{ΔN}$-α fused F_oF_1 has multiple, two on average, peripheral stalks and a-subunits.

Functional analysis of the H⁺/ATP ratio

We attempted to determine the H⁺/ATP ratio of the $δ_{ΔN}$-α fused F_oF_1 through biochemical measurements of the thermodynamic equilibrium between *pmf* and $ΔG'_{ATP}$, as previously reported[17]. Firstly, we prepared the F_oF_1-reconstituted proteoliposomes (PLs) and incubated them in an acidic buffer. The PLs were injected into the base assay medium to initiate ATP synthesis. The ATP synthesis/hydrolysis activity was monitored with the luciferin/luciferase assay system under various *pmf* conditions, with a given reaction quotient, Q ($= [ATP]/([ADP] \cdot [Pi])$). Figure 4a shows the time courses of the assay, in which the initial rate was determined. Figure 4b shows the reaction rates plotted against the *pmf* when $Q = 2.5$. The $δ_{ΔN}$-α fused F_oF_1 was shown to catalyze the ATP synthesis reaction even at low *pmf*, at which wild-type F_oF_1 is unable to synthesize ATP. For a more quantitative analysis, the data points were fitted with an exponential function to determine the equilibrium *pmf* (pmf_{eq}), where the torques of F_1 and F_o are balanced and the net reaction rate is zero. At the condition of Fig. 4b where $Q = 2.5$, pmf_{eq} was determined to be 68 mV for the $δ_{ΔN}$-α fused F_oF_1 and 133 mV for the wild-type. Thus, the minimum *pmf* for ATP synthesis was halved for the $δ_{ΔN}$-α fused F_oF_1, suggesting that the functional H⁺/ATP ratio of the $δ_{ΔN}$-α fused F_oF_1 is also doubled, in agreement with SDS-PAGE analysis. For further confirmation, we determined the pmf_{eq} at various Q values (Supplementary Fig. 3). Under all conditions, the pmf_{eq} of the $δ_{ΔN}$-α fused F_oF_1 was nearly half that of the wild-type.

Fig. 3 | Subunit stoichiometry of $\delta_{\Delta N}$-α fused F_oF_1. a SDS-PAGE analysis of the purified wild-type (WT) *Bacillus* PS3 F_oF_1 and the $\delta_{\Delta N}$-α fused F_oF_1. Each sample was derived from a single purification batch. 3 μg of F_oF_1 was loaded in each lane. The molecular masses of the $\delta_{\Delta N}$-α, α, β, γ, a, δ, b, $\varepsilon_{\Delta C}$, and c-subunits are 63, 55, 53, 32, 26, 20, 19, 9, and 7 kDa, respectively. The experiment was independently repeated three times with similar results. **b** The band intensity vs total protein amount. A single series of diluted F_oF_1 from the same purification batch was loaded into a gel and subjected to SDS-PAGE analysis. The band intensity of each subunit was plotted against the total amount of F_oF_1 loaded for SDS-PAGE analysis. The plots were fitted with a linear function. The slopes for γ (black), a- (red), and b-subunits (blue) were determined to be 2082, 502, and 2004 (arb. units/μg) for the WT F_oF_1, and 1521, 821, and 2675 (arb. units/μg) for the $\delta_{\Delta N}$-α fused F_oF_1, respectively. By normalizing the slopes of the a- and b-subunits to the slope of the γ subunit of each F_oF_1, the stoichiometries of the a- and b-subunits of the $\delta_{\Delta N}$-α fused F_oF_1 were estimated to be 2.2 (= (821/1521)/(502/2082)) and 1.8 (= (2675/1521)/(2004/2082)) times higher than those of the wild-type F_oF_1, respectively.

For the comprehensive analysis of the functional H^+/ATP ratio, Eq. (2) was transformed as below,

$$\Delta G' = \Delta G'_{ATP} - nF \cdot pmf = \Delta G^{0'}_{ATP} + 2.3RT \cdot \log Q - nF \cdot pmf_{eq} = 0 \quad (4)$$

$$2.3RT \cdot \log Q = -\Delta G^{0'}_{ATP} + nF \cdot pmf_{eq} \quad (5)$$

where $\Delta G^{0'}_{ATP}$ is the Gibbs free energy of ATP synthesis under the biochemical standard state, R and T are the gas constant and absolute temperature, respectively. Here, pmf_{eq} values were experimentally determined under defined Q conditions. The other values are constant. Therefore, when $2.3RT \cdot \log Q$ is plotted against $F \cdot pmf_{eq}$, n (= the H^+/ATP ratio) is determined as the slope of the data points. In addition, G^0_{ATP} is determined as the interception of the y axis. As shown in Fig. 4c, the $\delta_{\Delta N}$-α fused F_oF_1 exhibited a significantly steeper slope compared to the wild-type F_oF_1. From the linear fitting, the H^+/ATP ratio was determined to be 5.8 ± 0.4 and 3.0 ± 0.2 (fitted value ± SE of the fit) for the $\delta_{\Delta N}$-α fused F_oF_1 and wild-type, respectively. Although the H^+/ATP ratio of the wild-type is slightly lower than the structurally expected value of 3.3 and the reported value (3.3 ± 0.1)[17], $\delta_{\Delta N}$-α fused F_oF_1 was shown to double the H^+/ATP ratio, in close agreement with the subunit stoichiometry analysis from SDS-PAGE. This agreement suggests that the $\delta_{\Delta N}$-α fused F_oF_1 has two functional a-subunits in the ensemble average. From the interception of the y axis, the ΔG^0_{ATP} values are determined to be 38 ± 3 kJ mol^{-1} (fitted value ± SE of the fit) for both. This value shows a fine agreement with the reported values for *Bacillus* PS3 F_oF_1 (39 ± 1 kJ mol^{-1})[17], *E. coli* (38 ± 3 kJ mol^{-1})[18], yeast (36 ± 3 kJ mol^{-1})[19], and chloroplasts (38 ± 3 and 37 ± 3 kJ mol^{-1})[18,19], supporting the validity of the experiment.

Cryo-EM structural analysis
We determined the structure of the $\delta_{\Delta N}$-α fused F_oF_1 by single-particle cryo-EM analysis. The purified $\delta_{\Delta N}$-α fused F_oF_1 in detergent was applied to EM grids, frozen in liquid ethane, and imaged with 300 kV cryo-EM followed by single-particle analysis using cryoSPARC. The cryo-EM map was obtained by ab initio 3D reconstruction and classification, followed by refinement with C1 symmetry. Since the rotor complex in F_oF is oriented at one of the three catalytic dwell angles relative to the stator ring and peripheral stalk, alignment against the central core complex, including the rotor complex, revealed three distinct positions of the peripheral stalk, each separated by 120°, as observed in previous reports[25,26]. Map structure classification was performed by masking the peripheral-stalk positions, confirming the presence or absence of the peripheral stalk at the masked position (Supplementary Fig. 4). This classification was conducted for each stalk position: Stalks 1, 2, and 3. Thus, the map structure was classified into eight sub-classes. The overall resolution was 2.5–3.2 Å (Supplementary Fig. 4). While the wild-type F_oF_1 contains only a single peripheral stalk, this structural classification confirmed that some fractions of the particles contained multiple peripheral stalks (Fig. 5 and Supplementary Fig. 4). A significant fraction of the particles, however, had either no peripheral stalk or only a single one. The percentages of F_oF_1 structures with 0, 1, 2, and 3 peripheral stalks, as determined from the 3D classification, were 15, 51, 26, and 8%, respectively. Because of the lower resolution of the F_o region, focused refinement with F_o was conducted by masking the F_o region. The refined structure achieved resolutions of 3.5–6.6 Å, confirming that the peripheral stalk always accompanies F_o a-subunits (Supplementary Fig. 4). Thus, the percentage of F_oF_1 with 0, 1, 2, and 3 a-subunits should correspond to that for peripheral stalks. The fractions of F_oF_1 with multiple a-subunits were small, and the ensemble average of peripheral stalk was only 1.26 per molecule, which is evidently lower than the expected value of ~2 per molecule based on the subunit stoichiometry analysis and the functional analysis of H^+/ATP ratio. Although the exact reason for this discrepancy is unclear, it is highly likely that the peripheral stalk and the a-subunit dissociated due to the meniscus force
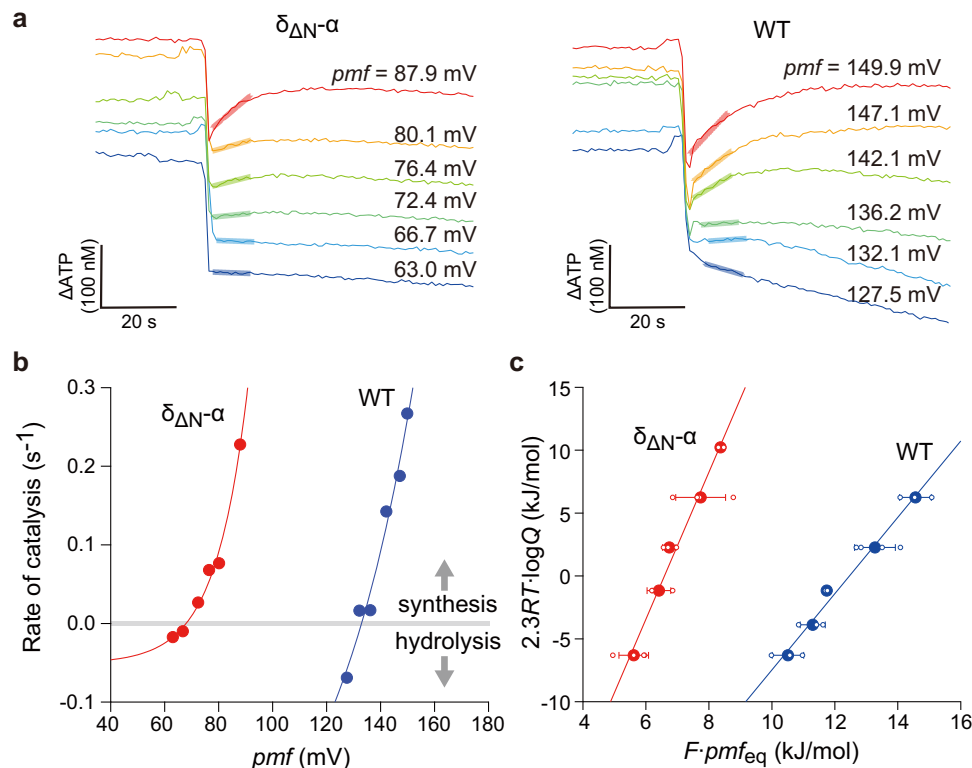
Fig. 4 | Functional analysis for the determination of the H⁺/ATP ratio. a Time courses of the ATP synthesis/hydrolysis activity of the reconstituted proteoliposomes (PLs) at different pmf. ATP synthesis reaction was measured using the luciferin/luciferase system. The reaction quotient, Q, was 2.5; [ATP] = 500 nM, [ADP] = 20 μM, [Pi] = 10 mM. The rate of catalysis was determined from the initial slopes (bold lines). **b** The ATP synthesis/hydrolysis rates determined from (**a**) were plotted against pmf. The data points were fitted with an exponential function for the determination of the equilibrium pmf, pmf_{eq}, as the interception of the x axis.

c Determination of the H⁺/ATP ratio. The mean (filled circles) and the SD of $F \cdot pmf_{eq}$ values were determined from 3 to 4 independent biological replicates (open circles) at each Q condition using different batches of purified enzymes, and $2.3RT \cdot \log Q$ values were plotted against the corresponding $F \cdot pmf_{eq}$ values according to Eq. (5). Sample sizes (n) from left to right are: 3, 3, 3, 4, 3 (WT) and 4, 3, 3, 4, 3 ($\delta_{\Delta N}$-α). Each line represents a linear regression fit to the dataset obtained from each F_oF_1.
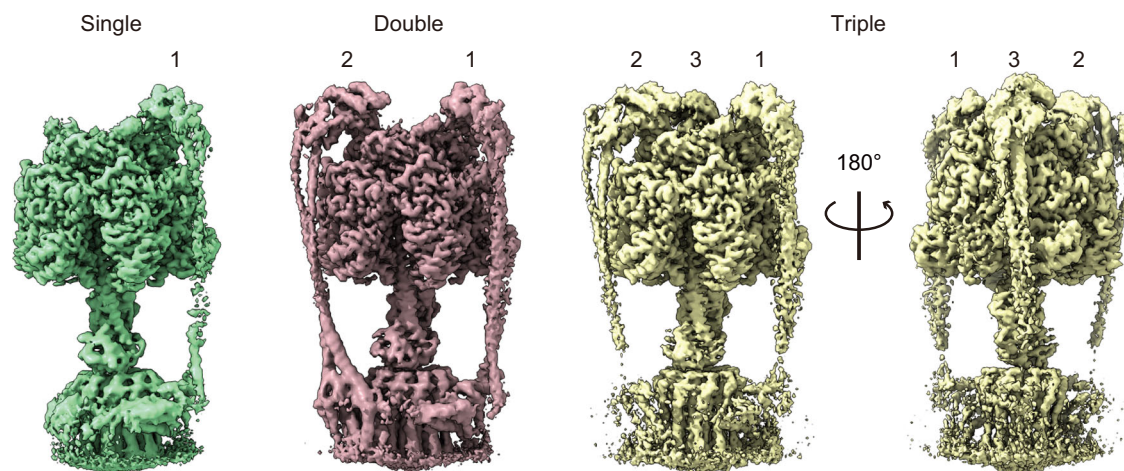

Fig. 5 | Cryo-EM maps of F_oF_1 with multiple peripheral stalks. The composite cryo-EM maps of F_oF_1 with single, double, and triple peripheral stalks. The number represents the position of each peripheral stalk. Scale bar, 25 Å.

and/or the interaction with the air/water interface during cryo-EM grid preparation[27].

Interaction between the peripheral stalk and the $\delta_{\Delta N}$-α fusion

Among the eight sub-classes, three structures contained a single copy of the peripheral stalk, each located at position Stalk 1, Stalk 2, or Stalk 3. These structures fit well with the reported three rotational state

structure of the wild-type *Bacillus* PS3 F_oF_1[25], respectively (Supplementary Fig. 5), indicating the structural integrity of the binding of the b_2 dimer to the F_1 part via $\delta_{\Delta N}$-α fusion. Slight differences were observed at the top of the F_1 headpiece and on the side of the central stalk because the $\delta_{\Delta N}$-α fused F_oF_1 lacks the N-terminal region of the δ subunit and the C-terminal helix of the ε subunit. The maps of the double- and triple-stalk F_oF_1 were compared with the corresponding
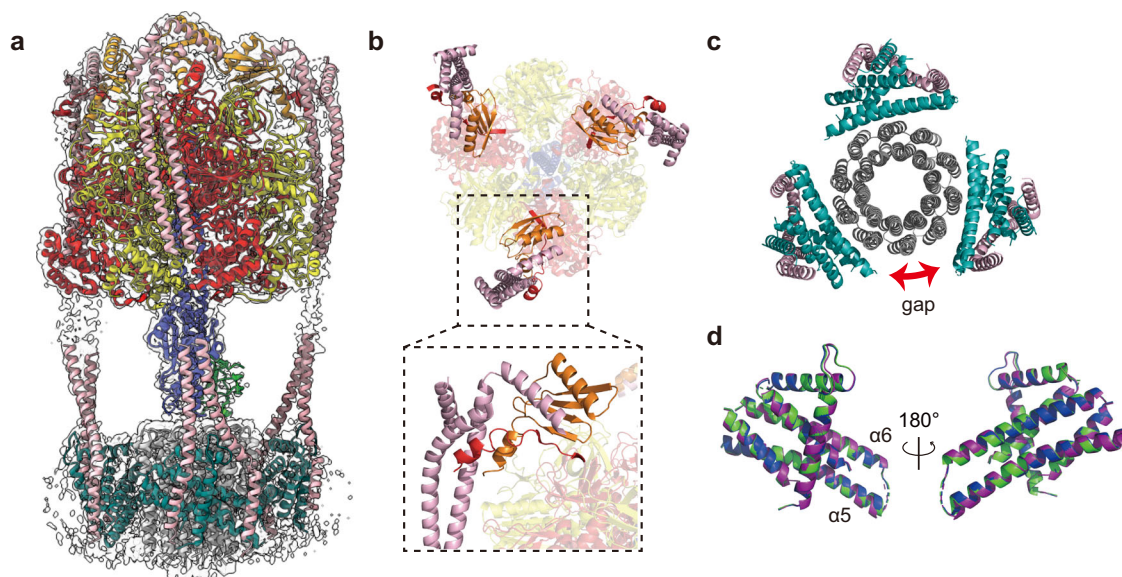
Fig. 6 | Atomic models of F_oF_1 with triple peripheral stalks. a Composite map and atomic models for the F_1 and F_o regions of the triple-stalk F_oF_1. The middle regions of the b-subunits could not be modeled due to the lack of clear density. **b** The top view of the structure. The close-up view shows the side view of the interaction between $\delta_{\Delta N}$-α fusion and the b_2 dimer. **c** The view from the bottom of the structure shown in (**a**). **d** The superposition of the three a-subunits (green, purple, and blue) in the triple-stalk F_o.

maps of single-stalk F_oF_1, respectively (Supplementary Fig. 6). These maps were well fitted, indicating that multiple stalks have no significant structural constraints on the whole structure of F_oF_1.

The atomic models for triple-stalk F_oF_1 are shown in Fig. 6. The structure of the $\delta_{\Delta N}$-α fusion region was well resolved, providing atomic details of its binding site with the b_2 dimer (Fig. 6a, b). As designed, the three binding sites were almost identical, with structures similar to those found in wild type *Bacillus* PS3 F_oF_1[25] and other ATP synthases[28] (Supplementary Fig. 7a). These observations reveal that the three b_2 dimers are incorporated via the canonical interaction with $\delta_{\Delta N}$-*a* fusion, suggesting the integrity of the peripheral stalks of the $\delta_{\Delta N}$-α fused F_oF_1.

Structure of the a-subunits

The structure and the position of the a-subunits of the triple-stalk F_oF_1 were investigated by comparing them with those in the wild-type *Bacillus* PS3 F_oF_1[25] (Fig. 6c and Supplementary Fig. 7b). The spatial intervals between the a-subunits are not perfectly symmetric because of the symmetry mismatch between the ring structures of F_1 and F_o, that is, threefold versus tenfold. Each a-subunit interacted with three neighboring c-subunits, forming an a_1c_3 unit. Therefore, a total of nine c-subunits interacted with the a-subunits, leaving the remaining c-subunit at the open position (gap) between two a-subunits (Fig. 6c). As a result, the three a-subunits were not positioned exactly 120° apart from each other. The asymmetric positioning of the a-subunits is in good agreement with that suggested by the three states of the wild-type *Bacillus* PS3 F_oF_1[25]. When the a-subunits in the triple-stalk F_oF_1 were compared to each other, Cα-RMSDs were 0.3−0.5 Å (Fig. 6d). In addition, the Cα-RMSDs estimated by superimposition of each a-subunit in the triple-stalk F_oF_1 with that in the corresponding state of the wild-type F_oF_1 were 0.9−1.0 Å. Moreover, superimposing the a_1c_3 units in the same manner yielded Cα-RMSDs of 1.0−1.2 Å (Supplementary Fig. 7c). Thus, at the current resolution, the overall structures of the three a-subunits in the triple-stalk F_oF_1 were essentially identical to each other and closely resembled that of the wild-type *Bacillus* PS3 F_oF_1. This suggests that all a-subunits are functional, which is consistent with the aforementioned biochemical analyses showing the enhanced H⁺/ATP ratio.

Structure of F_1 part

The structure of the F_1 portion of the triple-stalk F_oF_1 was investigated by comparing it with previously reported structures. The F_1 structure was found to be very similar to that of the *Bacillus* PS3 F_oF_1-$\varepsilon_{\Delta C}$ under uni-site catalysis conditions[26], with one β subunit bound to ADP in a closed conformation (β_{TP}^C) and two β subunits without bound nucleotide adopting open conformations (β_E^O, β_{DP}^O) (Supplementary Fig. 8a, b). The purified $\delta_{\Delta N}$-α fused F_oF_1 was prepared in nucleotide-free conditions. Therefore, it is highly likely that the bound ADP was endogenous. Notably, at a low-density threshold, weak map density was observed at the outer periphery of β_{TP}^C, which can be well fitted with the open β conformation of the nucleotide-depleted F_1 in the *Bacillus* PS3 F_oF_1-$\varepsilon_{\Delta C}$[26] (Supplementary Fig. 8c). This suggests that the cryo-EM map includes two conformations: closed and open. Other sub-class structures also exhibited similarly mixed maps.

Discussion

The present study provides insights into the design principles of ATP synthases using an engineering approach. Firstly, the δ subunit is the factor that defines the number of peripheral stalks. In this study, the N-terminal domain of δ, which breaks the structural pseudo-threefold symmetry by binding to the position on the symmetry axis, was deleted, and the C-terminal domain of δ was genetically fused to the N-terminal of the α subunit. As a result, up to three peripheral stalks were incorporated into the F_oF_1 complex. Structural analysis using cryo-EM revealed that the $\delta_{\Delta N}$-α fusion and the b_2 dimer adopted the canonical binding structure observed in the wild-type F_oF_1, except for the missing N-terminal domain of the δ subunit. This observation clearly shows that the N-terminal domain of the δ subunit determines the number of peripheral stalks per F_oF_1, restricting it to one by disrupting the structural symmetry.

Next, the number of a-subunits is determined based on the number of peripheral stalks. While cryo-EM analysis showed that some molecules lost peripheral stalks due to the detachment of the b_2 dimer, the observed peripheral stalks always remained bound to the a-subunits, indicating stable binding between the a-subunit and the b_2 dimer. Thus, the number of peripheral stalks determines the number of a-subunits. The structure of the triple-stalk F_oF_1 clearly showed that the c_{10} ring can accommodate up to three a-subunits, but not more

than four due to spatial constraints. Considering that each a-subunit can interact with three c-subunits, accommodating four or more a-subunits in F_oF_1 would require the c-ring consisting of more than 12 c-subunits, along with further engineering on the F_1 part, such as introducing a peripheral interaction site at the N-terminus of the β-subunit.

Another important finding of this study is the functional independence of the a-subunit, at least in terms of the coupling stoichiometry of H^+ (see below). In the triple-stalk F_oF_1, all three a-subunits interacted with the c-ring. In addition, the structural features of the interaction agreed well with those observed in the wild-type F_oF_1 structures. This suggests that each of the three a-subunits is functional. SDS-PAGE analysis revealed that the samples used in this study had an average of two peripheral stalks and two a-subunits. Consistent with these results, analysis of the equilibrium *pmf* revealed an H^+/ATP ratio that was doubled compared to that of the wild type. These results indicate that the coupling stoichiometry of the H^+ ions is proportional to the number of a-subunits. The additivity in H^+ stoichiometry means that each a-subunit tightly couples H^+ translocation and rotation of the c-ring, regardless of the presence of other a-subunits. This is consistent with the half-channel model, which assumes that the probability of H^+ translocation between the a and the c-subunits depends primarily on the relative position of these subunits, which explains well the functional independence of the a-subunits. Based on these considerations, we propose that the number of H^+ ions transported coupled with rotation is determined not only by the number of c-subunits constituting the c-ring but also by the number of a-subunits as follows:

$$N_{H^+/turn} = N_c \times N_a \qquad (6)$$

where $N_{H^+/turn}$, N_c, and N_a represent the total number of H^+ ions per turn, the number of c-subunit in the c-ring, and the number of a-subunit in F_o, respectively. However, one might point out the inconsistency between the biochemical results and the structural analysis with cryo-EM. The proportion of molecules with three peripheral stalks was extremely low, clearly lower than the average number suggested by the biochemical results. This is attributable to the dissociation of the peripheral stalks during sample preparation for cryo-electron microscopy. To confirm this point, it is necessary to develop multi-stalk F_oF_1 in which peripheral stalks stably bind to F_1 and to more accurately analyze the correlation between the number of the a-subunit and the H^+ stoichiometry.

As mentioned above, the increased H^+/ATP ratio suggests the functional independence of the a-subunits. However, this does not guarantee kinetic independence among the a-subunits. Thus, an arising question is: 'Can F_o with multiple a-subunits rotate the c-ring at the same rate as the wild-type F_o?'. In other words, 'Do the a-subunits conduct H^+ translocation without mutual interference?' This is a reasonable question considering that, before each 36° rotation step of the c-ring, all a-subunits must complete the H^+ translocation with the interacting c-subunits. Therefore, the time constant for each 36° rotation step is expected to be proportional to the number of a-subunits, meaning that the rate constant would decrease inversely.

Our biochemical experiments suggest that ATP hydrolysis-coupled proton pump activity was lower than that of the wild type (Supplementary Table 1). This aligns with the above expectation. However, other scenarios are possible: the engineered F_oF_1 may be more susceptible to the *pmf* progressively generated upon proton transport, and the engineered F_oF_1 may affect the catalytic activity of F_1. Therefore, a quantitative and systematic analysis is necessary to verify this issue.

Regarding the lower activity of the mutant, a naive question could arise: 'Why can the mutant still carry out the ATP synthesis reaction under lower *pmf* conditions despite its lower activity?'. The reason is as follows: the *pmf* required for F_oF_1 to synthesize ATP is determined by the pmf_{eq} at which the synthesis and hydrolysis reaction rates are balanced. The present study shows that the engineered F_oF_1 with multiple a-subunits doubles the H^+/ATP ratio, resulting in a halved pmf_{eq}. Therefore, although the engineered ATP synthase has lower catalytic activity, the mutant enzyme can continue the ATP synthesis reaction under low *pmf* conditions where the wild-type enzyme is unable to synthesize ATP.

This study has shown that, in principle, ATP synthase has the capacity to expand its H^+/ATP ratio to more than double. To date, experimentally confirmed H^+/ATP ratios of F_oF_1 have only been ~3–4. Even structural estimates suggest that 5.0 is the maximum for photosynthetic bacteria. Regarding this point, an N-type ATPase—considered a subtype of the F-type—has been reported to have an exceptionally large c-ring composed of 17 c-subunits[29]. Although the function and overall structure of this enzyme remain unknown, its predicted H^+/ATP ratio is 5.7. The present study demonstrates that the H^+/ATP ratio can be significantly increased by genetically engineering ATP synthase to increase the number of a-subunits, without resorting to such a large c-ring. Such genetic mutations may have arisen over the course of evolution. Indeed, we found that the gene operon of ATP synthase from *Acidaminococcus fermentans* shows the gene fusion of the δ and the α subunits (Supplementary Fig. 9). In addition, the N-terminal domain of δ is missing. These features are well consistent with the $δ_{ΔN}$-α fused F_oF_1 we designed. Thus, it is highly likely that *A. fermentans* F_oF_1 has a multi-stalk structure and can synthesize ATP under low *pmf* conditions. We also found that other species show similar features (UniProt ID: G4Q3K6, A0A1I2C5T3), suggesting more possibility of a multi-stalk F_oF_1 in nature. Thus, the present study suggests the unexpected diversity in the design principles of the F_oF_1 ATP synthase, which awaits further experimental verification.

From an engineering standpoint, the findings of the present study may provide future directions for cell engineering. So far, in microbial fermentation, attention has primarily been devoted to developing metabolic pathways and altering metabolic fluxes, while little effort has been made to optimize the intracellular concentrations and ratios of NAD(P)H and ATP, which are fundamental to cellular bioenergetics. When ATP synthesis is driven by oxidative phosphorylation, the amount of ATP produced depends on the extent of NADH oxidation. In such cases, an increase in the H^+/ATP ratio translates into a higher NADH/ATP ratio. This could have a significant impact on microbial fermentations. In particular, it could enhance bioproduction in photosynthetic bacteria when ATP is the bottleneck factor[22,30]. To verify this possibility, it will be necessary to investigate how introducing ATP synthase with a modified H^+/ATP ratio affects cell growth and product formation. Additionally, such insights are likely to shed light on the physiological role of naturally occurring multi-stalk F_oF_1, which may also exist in nature.

Methods

Preparation of F_oF_1
In this study, *Bacillus* PS3 F_oF_1-$ε_{ΔC}$, which has a 10× His-tag at the N-terminus of the β subunit and lacks the inhibitory C-terminal domain of the ε subunit[17,24] was used as the wild-type. The engineered $δ_{ΔN}$-α fusion construct of *Bacillus* PS3 F_oF_1-$ε_{ΔC}$ lacks the full-length δ subunit and has a $δ_{ΔN}$-α fused subunit in which the N-terminal domain (residues 2–104) of the δ subunit is deleted and its C-terminus is fused to the N-terminus (without Met) of the α subunit via a short linker. The wild-type and engineered F_oF_1s were expressed in *E. coli* DK8 cells, which lack endogenous F_oF_1 genes, by incubating in Super broth at 37 °C for 20 h. Cultured cells were suspended in a solution (10 mM HEPES, pH 7.5, 5 mM MgCl$_2$, and 10% (v/v) glycerol) and disrupted by sonication. After removing the cell debris at 9100 × *g* for 45 min, membrane fraction was collected by centrifugation for 131,500 × *g* for 1 h at 4 °C. F_oF_1 was solubilized from the membrane fraction by adding 0.5% (w/v) LMNG (NG310; Anatrace, USA) and incubating for 30 min at 30°C. After centrifugation at 162,000 × *g* for 30 min, the solubilized

fraction was applied to a Ni-Sepharose column pre-equilibrated with M buffer (20 mM potassium phosphate buffer and 100 mM KCl, pH 7.5) containing 0.005% LMNG. The column was washed with M buffer containing 20 mM imidazole and 0.005% LMNG, and F_oF_1 was eluted with M buffer containing 200 mM imidazole and 0.005% LMNG. The eluted F_oF_1 fractions were concentrated before being applied to a Superdex 200 Increase 10/300 column (Cytiva) equilibrated with gel filtration buffer (20 mM HEPES, pH7.5, 100 mM NaCl, and 0.005% LMNG). The peak fractions corresponding to F_oF_1 were collected and concentrated to 5–10 mg/mL, frozen with liquid nitrogen, and stored at −80 °C until use. The protein concentrations were determined using a BCA protein assay kit (Pierce) with bovine serum albumin as a standard. The molecular weight of the protein was calculated based on the sequence and subunit stoichiometry. For the $\delta_{\Delta N}$-α fused F_oF_1, the molecular weight was calculated assuming an average of two peripheral stalks per F_oF_1 molecule.

Measurement of ATP synthesis/hydrolysis activity of F_oF_1
ATP synthesis/hydrolysis activity of F_oF_1 was measured using a luciferin-luciferase system at 25 °C, as described previously[17]. F_oF_1-reconstituted PLs were prepared as described[17]. Then, 300 μL of the PLs were mixed with 700 μL of acidic buffer containing 50 mM MES or HEPES buffer, 0.143–14.3 mM NaH_2PO_4, 6.7 mM KCl, 49 mM NaCl, 4 mM $MgCl_2$, and 600 mM sucrose and NaOH to obtain the desired pH, and then ADP and valinomycin were added to a final concentration of 20–640 μM and 200 nM, respectively. After incubation for 10–24 h at 25 °C for acidification, base assay medium was prepared by mixing 25 μL of the luciferin/luciferase mixture (2× concentration of CLSII solution in ATP bioluminescence assay kit, Roche, and 5 mM luciferin), 800 μL of the base buffer (380 mM HEPES buffer, 0.1125–11.25 mM NaH_2PO_4, 5.63 mM KCl, 55 mM NaCl, 4 mM $MgCl_2$, KOH to adjust K^+ concentration and NaOH to adjust pH), 50-100 μL of ATP and ADP to obtain the desired concentration, and water to adjust the total volume to 900 μL and incubated for 10 min for equilibrium. Then, the 100 μL of acidified PLs was injected into the base assay medium to initiate the ATP synthesis reaction, and the ATP synthesis/hydrolysis activity was monitored with the luciferin/luciferase assay system using a luminometer (Luminescencer AB2200, ATTO). For calibrating luminescence light intensity to ATP concentration, 10 μL of 10 μM ATP was added. The rate was determined from the initial slope of the linear regression of the time courses. The ΔpH was obtained by subtracting pH_{in} from pH_{out}, which was determined by directly measuring the pH using a glass electrode. Transmembrane electrical potential, $\Delta\psi$, was estimated from the Nernst equation.

Other assays
SDS-PAGE analysis was performed with 10–20% (w/v) gradient gels. The gels were stained with Coomassie Brilliant Blue (CBB Stain One Super, Nacalai Tesque, Japan) and imaged with a ChemiDoc Imaging System (BIORAD, USA). The band intensity of each subunit was measured using the gel analyzer tool of Fiji (ImageJ 1.54 f) software. ATPase activity measurements of PLs using an ATP regeneration system were performed at 25 °C in the ATPase assay solution (50 mM HEPES-KOH, pH 7.5, 100 mM KCl, 5 mM $MgCl_2$, 2 mM ATP, 1 μg/ml Carbonyl cyanide-p-trifluoromethoxyphenylhydrazone, 2.5 mM phosphoenolpyruvate, 100 μg/mL lactate dehydrogenase, 100 μg/mL pyruvate kinase and 0.2 mM NADH) as described previously[31]. ATP-driven H^+-pumping activity was measured by quenching of ACMA (9-amino-6-chloro-2-methoxyacridine) fluorescence at 25 °C in PA4 buffer (10 mM HEPES-KOH, pH 7.5, 100 mM KCl, 5 mM $MgCl_2$) supplemented with 0.3 μg/ml ACMA and 1.0 μg/ml F_oF_1-reconstituted PLs[31].

Cryo-EM grid preparation and data collection
After adding 0.05% lysophosphatidylcholine (1-palmitoyl-2-hydroxy-sn-glycero-3-phosphocholine), 3.0 μL of purified protein (3–6 mg/mL) was loaded onto the glow-discharged Quantifoil R1.2/1.3 grids using a Vitrobot Mark IV (Thermo Fisher Scientific). Grids were blotted for 5 s with a blotting force of 15 under 100% humidity at 18 °C, and flash-frozen in liquid ethane. Data were collected using a 300 kV Titan Krios electron microscope (Thermo Fisher Scientific) with a Falcon 4i direct detector device camera with Selectris-X automated with EPU software. Images were recorded in electron counting mode by recording 50 movie frames with an exposure rate of 1.0 e$^-$/Å^2 per frame. The defocus range was 0.8–2.0 μm, and the original pixel size was 0.75 Å.

Cryo-EM data processing
All image processing steps were performed using cryoSPARC v4.3.0. Details of the image processing workflow are described in Supplementary Fig. 4. A total of 56,081 micrographs were first motion corrected, and the CTF was estimated by patch CTF estimation. Particles were manually picked, and templates for particle selection were generated from 2D classification. After template picking, the selected 4,316,627 particles were subjected to 2D classification. Then, further selections with ab initio 3D reconstruction, heterogeneous, homogeneous, and non-uniform refinements were performed. After non-uniform refinement, all particles were sequentially subjected to a focused 3D refinement using masks for each of the three peripheral stalks, including the N-terminal region of the α subunit, the C-terminal region of the δ subunit and the hydrophilic region of the b_2-subunits. Each mask was generated from three rotational states of wild-type *Bacillus* PS3 F_oF_1 (PDBs 6N2Z, 6N30, and 6N2Y). Eight classes, including one to three peripheral stalks and three rotational states of F_oF_1, were identified. The three datasets were collected, merged and refined with non-uniform refinement, resulting in an overall resolution of 2.5–3.2 Å. Further refinement with the F_o mask resulted in a map of the F_o region with an improved resolution of 3.5–6.6 Å. The resolution was estimated using the FSC criterion of 0.143 threshold. The cryo-EM data collection and refinement statistics are shown in Supplementary Tables 2 and 3. The local resolution maps, FSC curves, orientation distribution plots and Model-to-map fits are shown in Supplementary Figs. 10–12.

Model building
Models were built and refined in COOT v0.9.8.93 and PHENIX v1.20.1-4487. using PDB 6N2Z, 6N30, and 6N2Y as the initial model. Validation statistics are shown in Supplementary Tables 2 and 3. A composite map was generated by combining the F_1 region of the triple-stalk F_oF_1 map and the F_o map obtained through local refinement with the F_o mask, using UCSF ChimeraX v1.8 for illustration purposes only. Figures were prepared using PyMOL v2.4.0&2.5.2, UCSF Chimera v1.17.3, and UCSF ChimeraX v1.5&1.8. RMSD values for Cα-atoms were calculated using PyMOL 2.4.0 align command without outlier rejection.

Reporting summary
Further information on research design is available in the Nature Portfolio Reporting Summary linked to this article.

Data availability
The cryo-EM maps and models generated in this study were deposited to EMDB and PDB under the following accession codes: EMD-61339; EMD-61340; EMD-61341; EMD-61342; EMD-61343; EMD-61344; EMD-61345; EMD-61346; EMD-61347; EMD-61348; EMD-61349; EMD-61350; EMD-61351; EMD-61352; EMD-61353; EMD-61354, and 9JC1; 9JC2. Previously published structures used in this study are also available from PDB under the following accession codes: 6N2Z; 6N30, and 6N2Y. Source data are provided with this paper.

References
1. Walker, J. E. The ATP synthase: the understood, the uncertain and the unknown. *Biochem. Soc. Trans.* **41**, 1–16 (2013).

2. Boyer, P. D. The ATP synthase-a splendid molecular machine. *Annu. Rev. Biochem.* **66**, 717–749 (1997).

3. Yoshida, M., Muneyuki, E. & Hisabori, T. ATP synthase-a marvellous rotary engine of the cell. *Nat. Rev. Mol. Cell Biol.* **2**, 669–677 (2001).

4. Guo, H. & Rubinstein, J. L. Cryo-EM of ATP synthases. *Curr. Opin. Struct. Biol.* **52**, 71–79 (2018).

5. Kuhlbrandt, W. Structure and mechanisms of F-Type ATP synthases. *Annu Rev. Biochem.* **88**, 515–549 (2019).

6. Stewart, A. G., Laming, E. M., Sobti, M. & Stock, D. Rotary ATPases-dynamic molecular machines. *Curr. Opin. Struct. Biol.* **25**, 40–48 (2014).

7. Abrahams, J. P., Leslie, A. G., Lutter, R. & Walker, J. E. Structure at 2.8 A resolution of F1-ATPase from bovine heart mitochondria. *Nature* **370**, 621–628 (1994).

8. Noji, H., Yasuda, R., Yoshida, M. & Kinosita, K. Jr. Direct observation of the rotation of F1-ATPase. *Nature* **386**, 299–302 (1997).

9. Itoh, H. et al. Mechanically driven ATP synthesis by F1-ATPase. *Nature* **427**, 465–468 (2004).

10. Rondelez, Y. et al. Highly coupled ATP synthesis by F1-ATPase single molecules. *Nature* **433**, 773–777 (2005).

11. Vik, S. B. & Antonio, B. J. A mechanism of proton translocation by F1F0 ATP synthases suggested by double mutants of the a subunit. *J. Biol. Chem.* **269**, 30364–30369 (1994).

12. Junge, W., Lill, H. & Engelbrecht, S. ATP synthase: an electro-chemical transducer with rotatory mechanics. *Trends Biochem. Sci.* **22**, 420–423 (1997).

13. Allegretti, M. et al. Horizontal membrane-intrinsic alpha-helices in the stator a-subunit of an F-type ATP synthase. *Nature* **521**, 237–240 (2015).

14. Watt, I. N., Montgomery, M. G., Runswick, M. J., Leslie, A. G. W. & Walker, J. E. Bioenergetic cost of making an adenosine triphosphate molecule in animal mitochondria. *Proc. Natl. Acad. Sci. USA* **107**, 16823–16827 (2010).

15. Ferguson, S. J. ATP synthase: From sequence to ring size to the P/O ratio. *Proc. Natl. Acad. Sci. USA* **107**, 16755–16756 (2010).

16. Stock, D., Leslie, A. G. W. & Walker, J. E. Molecular architecture of the rotary motor in ATP synthase. *Science* **286**, 1700–1705 (1999).

17. Soga, N., Kimura, K., Kinosita, K. Jr., Yoshida, M. & Suzuki, T. Perfect chemomechanical coupling of F(o)F(1)-ATP synthase. *Proc. Natl. Acad. Sci. USA* **114**, 4960–4965 (2017).

18. Steigmiller, S., Turina, P. & Graber, P. The thermodynamic H+/ATP ratios of the H+-ATPsynthases from chloroplasts and Escherichia coli. *Proc. Natl. Acad. Sci. USA* **105**, 3745–3750 (2008).

19. Petersen, J., Forster, K., Turina, P. & Graber, P. Comparison of the H +/ATP ratios of the H+-ATP synthases from yeast and from chloroplast. *Proc. Natl. Acad. Sci. USA* **109**, 11150–11155 (2012).

20. Pogoryelov, D. et al. The oligomeric state of c rings from cyanobacterial F-ATP synthases varies from 13 to 15. *J. Bacteriol.* **189**, 5895–5902 (2007).

21. Preiss, L. et al. The c-ring stoichiometry of ATP synthase is adapted to cell physiological requirements of alkaliphilic Bacillus pseudofirmus OF4. *Proc. Natl. Acad. Sci. USA* **110**, 7874–7879 (2013).

22. Davis, G. A. & Kramer, D. M. Optimization of ATP synthase c-rings for oxygenic photosynthesis. *Front. Plant. Sci.* **10**, 1778 (2019).

23. Cheuk, A. & Meier, T. Rotor subunits adaptations in ATP synthases from photosynthetic organisms. *Biochem. Soc. Trans.* **49**, 541–550 (2021).

24. Masaike, T., Suzuki, T., Tsunoda, S. P., Konno, H. & Yoshida, M. Probing conformations of the beta subunit of F0F1-ATP synthase in catalysis. *Biochem. Biophys. Res. Commun.* **342**, 800–807 (2006).

25. Guo, H., Suzuki, T. & Rubinstein, J. L. Structure of a bacterial ATP synthase. *Elife* **8**, e43128 (2019).

26. Nakano, A., Kishikawa, J. I., Nakanishi, A., Mitsuoka, K. & Yokoyama, K. Structural basis of unisite catalysis of bacterial F(0)F(1)-ATPase. *PNAS Nexus* **1**, pgac116 (2022).

27. D'Imprima, E. et al. Protein denaturation at the air-water interface and how to prevent it. *Elife* **8**, e42747 (2019).

28. Spikes, T. E., Montgomery, M. G. & Walker, J. E. Structure of the dimeric ATP synthase from bovine mitochondria. *Proc. Natl. Acad. Sci. USA* **117**, 23519–23526 (2020).

29. Schulz, S., Wilkes, M., Mills, D. J., Kuhlbrandt, W. & Meier, T. Molecular architecture of the N-type ATPase rotor ring from Burkholderia pseudomallei. *EMBO Rep.* **18**, 526–535 (2017).

30. Nogales, J., Gudmundsson, S., Knight, E. M., Palsson, B. O. & Thiele, I. Detailing the optimality of photosynthesis in cyanobacteria through systems biology analysis. *Proc. Natl. Acad. Sci. USA* **109**, 2678–2683 (2012).

31. Suzuki, T., Ueno, H., Mitome, N., Suzuki, J. & Yoshida, M. F. 0) of ATP synthase is a rotary proton channel. Obligatory coupling of proton translocation with rotation of c-subunit ring. *J. Biol. Chem.* **277**, 13281–13285 (2002).

Acknowledgements

Author contributions

H.U., K.Y. and R.M. performed the biochemical experiments. N.H-S. and N.A. performed the cryo-EM analysis. T.S. and T.M. provided the technical support and conceptual advice. H.U. and H.N. conceived and supervised the study and wrote the manuscript. All the authors discussed the results and commented on the manuscript.

Competing interests

The authors declare no competing interests.

Additional information

Supplementary information The online version contains supplementary material available at
https://doi.org/10.1038/s41467-025-61227-w.

Correspondence and requests for materials should be addressed to Hiroshi Ueno or Hiroyuki Noji.

Peer review information *Nature Communications* thanks Yan Gao, Stephan Wilkens, and the other, anonymous, reviewer(s) for their contribution to the peer review of this work. A peer review file is available.

Reprints and permissions information is available at
http://www.nature.com/reprints